Thermohydrodynamics of boiling in a van der Waals fluid

T. Laurila,[1] A. Carlson,[2] M. Do-Quang,[2] T. Ala-Nissila,[1,3] and G. Amberg[2]

[1]*COMP CoE at the Department of Applied Physics, P.O. Box 11100, Aalto University School of Science, FI-00076 AALTO, Finland*
[2]*Linné Flow Center, Department of Mechanics, The Royal Institute of Technology, Stockholm, Sweden*
[3]*Department of Physics, Brown University, Providence, Rhode Island 02912-8143, USA*

We present a modeling approach that enables numerical simulations of a boiling Van der Waals fluid based on the diffuse interface description. A boundary condition is implemented that allows in and out flux of mass at constant external pressure. In addition, a boundary condition for controlled wetting properties of the boiling surface is also proposed. We present isothermal verification cases for each element of our modeling approach. By using these two boundary conditions we are able to numerically access a system that contains the essential physics of the boiling process at microscopic scales. Evolution of bubbles under film boiling and nucleate boiling conditions are observed by varying boiling surface wettability. We observe flow patters around the three-phase contact line where the phase change is greatest. For a hydrophilic boiling surface, a complex flow pattern consistent with vapor recoil theory is observed.

PACS number(s): 47.55.D−, 47.11.Fg, 44.35.+c, 64.70.fh

I. INTRODUCTION

Boiling and condensation are common phenomena in everyday life. Perhaps the most obvious examples are various processes during cooking, but an even more ubiquitous example would be weather phenomena due to the interplay of water, water vapor, and air. In engineering, boiling heat transfer is a common method of heat transfer in thermal power plants, conventional and nuclear alike, and is thus an indispensable part of electricity production. Efficiency of heat transfer by boiling is limited by the creation of a vapor film at the hot surface when heat throughput is too high [1–4]. This effect is generally called critical heat flux, boiling crisis, or dryout. The insulating effect of the vapor film causes a rapid and destructive jump in temperature at the newly dry wall.

While macroscopic and effective properties of boiling and condensation have been studied for centuries, and properties such as latent heats of materials are known in great detail, the dynamics of how boiling and condensation happens, especially the initial stages of the formation of bubbles or droplets, is still largely unresolved. A classical issue is heterogenous boiling and condensation, where the phase transition is macroscopically observed to occur at much smaller superheats than classical theories predict. The boiling crisis mentioned above is an example where understanding and thereby controlling the dynamics of bubbles as they form would have an obvious technological impact.

Observing in experiments the incipience of bubble nucleation in boiling is challenging, as the dynamics is inherently fast and occur on microscopic scales. The separation of time and length scales is significantly reduced when dealing with a liquid close to its critical point and in a microgravity environment, but this produces a host of challenges of its own [5,6]. Mathematically and computationally, thermal multiphase flow problems are challenging to describe [7–9]. To our knowledge, neither computational nor experimental observations have been reported of the microscopic flow around the three-phase contact line where boiling on a heated surface predominantly happens. The vapor recoil theory proposed by Nikolayev

and coworkers links the flow profile to the boiling crisis by presenting dryout as a single-bubble spreading event [10].

In his pioneering work on liquid-gas phase transitions, Van der Waals [11] considered the coexistence of liquid and gas to consist of a density field that attains two different values and varies smoothly but rapidly in between. Van der Waals also attributed a free energy cost to the gradients of the density field. These ideas have been extended for thermodynamics and hydrodynamics of nonuniform phases by, among others, Korteweg [12], Ginzburg and Landau [13], Cahn and Hilliard [14], and Dunn and Serrin [15]. The results of this work are in modern parlance called phase field methods or diffuse interface methods in the materials science and fluid dynamics communities, respectively.

Diffuse interface methods have received renewed attention in recent years, much of which can be attributed to the increased capabilities of modern computers enabling simulations of relevant problems by using these methods. A review of the contemporary diffuse interface methods was given by Anderson [7]. Recently, Onuki presented a new formulation [8]. These two have a difference in how the thermal gradient couples to stress at the interface, although as guiding principle both use the reversibility of capillary forces.

A number of numerical simulation studies have been performed considering condensation, boiling, drop spreading, bubbles, and droplets in nonuniform thermal fields [8,17–21]; however, all of these are made for systems that are enclosed by solid walls. A key factor in simulating the dynamics of boiling is that a bubble must be able to grow while the surrounding liquid maintains its metastable state. In a numerical simulation this means that there must be an open boundary on the computational domain that allows mass to either flow in or out, making the average density of the system change in time.

An ideal open boundary would not reflect any information of outgoing flow back into the computational domain [22]. Because sound waves are always present in the compressible system, this should particularly hold for the acoustic modes. In our work we observe the phase change between gas and liquid to cause compressibility waves. We assume that the

opposite phenomenon (i.e., sound waves affecting the phase change) is insignificant and can be ignored. Thus we neglect the acoustic properties of our boundaries, which leads to a significant simplification. The study presented here for diffuse interface boiling properly includes both the thermodynamics and hydrodynamics in an open system.

The aim here is to develop two separate boundary conditions, one that will allow us to control the wettability of the solid substrate and the other to allow mass flux through an open boundary enabling us to simulate boiling. The proposed modeling approach for the wetting boundary condition is adopted from the isothermal Cahn-Hilliard method [16]. Modeling of contact lines are particularly relevant in boiling, which is the final goal of the study presented in this article. The basis of the open boundary condition is simple thermodynamics, but we find it necessary to introduce pressure as an additional variable to make it work in practice.

Figure 1 presents a sketch of all the computational cases we study and as such presents an outline of the article. After presenting the mathematical model (Sec. II) and numerical formulation (Sec. III), we proceed to verify the model with various isothermal cases in Sec. IV. First we verify the Young-Laplace law for a bubble immersed in its liquid at
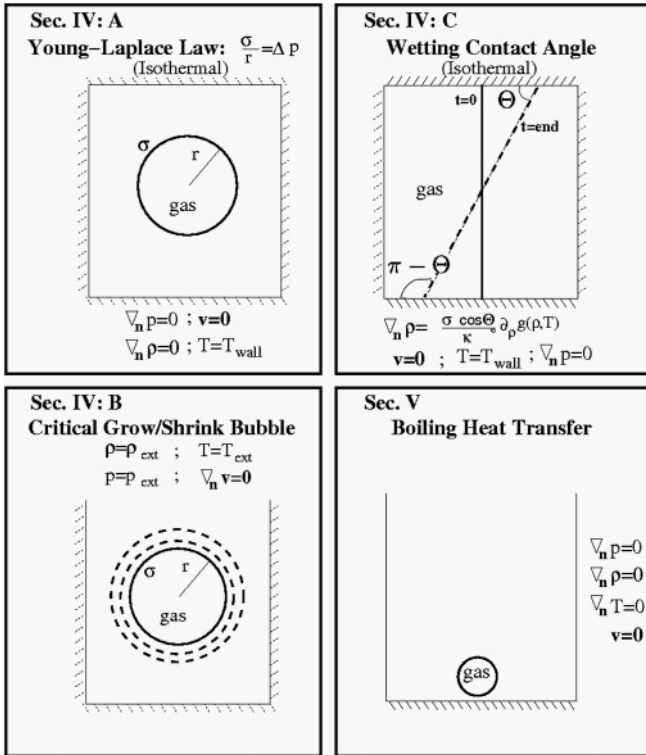

FIG. 1. Schematic view of the computational cases considered in this paper with corresponding boundary conditions. We simulate the Young-Laplace law for a single bubble immersed in its coexistence liquid. We verify the open boundary condition by comparing with an analytical solution. The proposed wetting boundary condition is verified in simulations of isothermal systems but for different temperatures. Numerical simulations of boiling are performed in a domain with a temperature gradient, where the upper boundary allows mass flux in and out.

coexistence. The case is illustrated in the upper-left panel in Fig. 1. To verify the open boundary condition we look at the growth or collapse of bubbles immersed in metastable liquid as function of their initial size. A theoretical estimate for limiting size is obtained from the Gibbs free energy, and numerical simulations sketched in lower-left panel of Fig. 1 are in good agreement with the prediction. A sketch of the numerical system that is used to verify the wetting condition is illustrated in the panel to the upper right in Fig. 1. Initially a straight interface is connected with two walls with the opposite equilibrium angle imposed. The equilibrium interface is straight and we measure the angle it takes between the two walls. In Sec. V we present numerical simulations of boiling dynamics of a Van der Waals fluid, where one of the boundaries is open. We show in particular the effect of the solid wettability on the rate of phase change from liquid to gas.

II. MATHEMATICAL MODEL

The Van der Waals (VdW) model of liquid-gas coexistence is described by the Helmholtz free energy per volume [8]:

$$f(\rho, T) = k_B T \frac{\rho}{m_p} \left[\ln \left(\frac{\frac{\rho}{m_p} T^{3/2}}{1 - b \frac{\rho}{m_p}} \right) - 1 \right] - a \left(\frac{\rho}{m_p} \right)^2. \quad (1)$$

The corresponding VdW equation of state is obtained as

$$p(\rho, T) = \rho \partial_\rho f(\rho, T) - f(\rho, T) = \frac{k_B T \frac{\rho}{m_p}}{1 - b \frac{\rho}{m_p}} - a \left(\frac{\rho}{m_p} \right)^2,$$

$$(2)$$

and the internal energy is obtained as

$$e(\rho, T) = f(\rho, T) - T \partial_T f(\rho, T) = \frac{3 k_B}{2m} T \rho - \frac{a}{m^2} \rho^2. \quad (3)$$

Above, we have the pressure p, mass density ρ, temperature T, Boltzmann constant k_B and molecular mass m_p. $\partial_\rho = \partial/\partial\rho$ is a short-hand notation for the partial derivative that we will keep throughout this article. The VdW parameters a and b describe the fluid in question. The scope of the present work is the qualitative description of the general thermodynamics and hydrodynamics of liquid-gas phase changes and, for this purpose, the VdW model provides a well-established benchmark. It should be noted that the VdW model might not be the most computationally convenient and efficient among the simple equations of state [27], but as the classic benchmark of a liquid-vapor phase transition it is the most appropriate choice for our purpose.

In addition to an equation of state with two stable phases, the description of two-phase coexistence needs to account for the interfaces between the phases. The central idea of the diffuse interface method; namely, that there is an energy cost associated with spatial change of an order parameter and the order parameter changes rapidly but smoothly across an interface, was considered already by Van der Waals [11]. In the case of the liquid-gas phase transition, the density plays the role of the order parameter. In modern guise, the diffuse

interface method starts with the free energy [16]

$$F = \int dx \left[f(\rho(x), T(x)) + \frac{\kappa}{2} |\nabla \rho(x)|^2 \right], \qquad (4)$$

where surface tension is described in terms of the gradient energy coefficient κ. The actual surface tension depends on κ and the form of the free energy density f, which must be of double tangent form as function of density [14]:

$$\sigma = \sqrt{2\kappa} \int_{\rho_g}^{\rho_l} d\rho \sqrt{\Delta f(\rho, T)}, \qquad (5)$$

where ρ_g and ρ_l are the gas and liquid densities at coexistence at temperature T. $\Delta f(\rho)$ is the difference between value of $f(\rho)$ and the double tangent line at ρ. This is valid when temperature is uniform across the interface. Different assumptions have been made on how $\kappa(\rho, T)$ depends on density and temperature [7,8,18,19]. κ couples to both the surface tension and the interface width and experimental data on κ as function of temperature and pressure is sparse. In this work we have made the simplest assumption that κ is constant, which can be determined so that the surface tension of our VdW fluid corresponds in order of magnitude to that of a real fluid. Qualitatively the surface tension behaves properly as a function of temperature and pressure, vanishing at the critical point and increasing below the critical point as a function of temperature and pressure.

Coexistence between the liquid and gas phases is obtained as a minimum of the free energy, constrained such that densities far away from the interface are ρ_l and ρ_g. Considering the case of constant temperature, the minima of the free energy are obtained via the Euler-Lagrange equation of the functional of Eq. (4). On the other hand, mechanical balance of the system is obtained from the stress tensor as zero divergence:

$$\partial_j P_{ij} = 0, \quad \text{for every } i. \qquad (6)$$

We use the Einstein summation notation and the shorthand notation $\partial_i = \partial/\partial_{x_i}$, and similarly for j and k. This zero stress divergence criterion, or zero force, corresponds to the Euler-Lagrange equation of F or minimum free energy if the stress tensor equals

$$P_{ij}^T = \left(p(\rho, T) - \kappa\rho\partial_k^2\rho - \tfrac{1}{2}\kappa\partial_k\rho\partial_k\rho \right)\delta_{ij} + \kappa\partial_i\rho\partial_j\rho. \qquad (7)$$

The above result for the stress tensor in constant temperature and constant κ is equivalent among the existing diffuse interface models [7,8,29].

The hydrodynamic equations for mass continuity and fluid motion with the stress tensor above read

$$\partial_t \rho + \partial_j(\rho v_j) = 0, \qquad (8)$$

$$\partial_t(\rho v_i) + \partial_j(\rho v_i v_j) = -\partial_j P_{ij}^T + \partial_j \sigma_{ij} + g_i, \qquad (9)$$

where σ_{ij} is the viscous stress and g_i includes external bulk forces such as gravity.

Considering full thermodynamics, that is a temperature field as function of time and space as well, the foundation of extending the isothermal model above has been to demand that interfacial forces due to the gradient energy work adiabatically. This can be obtained in two different ways, either as a flux of internal energy proportional to temperature gradients with Fourier's law in the energy conservation equation [7,29], or the pressure tensor itself is extended with terms proportional to temperature gradient [8].

The two-phase model must also account for diffusive transport of both heat and mass that changes between the two phases. This means incorporating a model for the viscosity (η) and thermal diffusivity coefficients (α) as a function of density. In this work we assume these material properties to be linearly proportional to the density; namely,

$$\eta = \eta_0 \rho, \qquad (10)$$

$$\alpha = \alpha_0 \rho, \qquad (11)$$

where η_0 and α_0 are constants.

For the two-dimensional (2D) simulations we present here, we use the model formulated by Onuki [8], which explicitly written out in our case takes the form

$$\partial_t \rho + \partial_j(\rho v_j) = 0, \qquad (12)$$

$$\partial_t v_i + \partial_j(\rho v_i v_j) = -\partial_j P_{ij} + \eta_0 \partial_j[\rho(\partial_i v_j + \partial_j v_i)] + \rho g_i, \qquad (13)$$

$$\begin{aligned} \partial_t e(\rho, T) &+ \partial_j(e(\rho, T)v_j) \\ &= -P_{jk}\partial_j v_k + \eta_0[\rho(\partial_j v_k + \partial_k v_j)]\partial_j v_k + \alpha_0 \partial_j(\rho\partial_j T), \end{aligned} \qquad (14)$$

$$\begin{aligned} P_{ij} &= \left(p(\rho, T) - \kappa\rho\partial_k^2\rho - \frac{1}{2}\kappa\partial_k\rho\partial_k\rho + \kappa\frac{\rho}{T}\partial_k\rho\partial_k T \right)\delta_{ij} \\ &\quad + \kappa\partial_i\rho\partial_j\rho. \end{aligned} \qquad (15)$$

Note that, above, we have applied the standard viscous stress tensor in 2D and identical bulk and shear viscosities, which we use in our simulations. Phase change is driven here by the nonequilibrium state of the system, which produces a large contribution in the stress tensor given in Eq. (15). Since this is a system of coupled equations, this gives a contribution into the momentum and then the mass conservation equation. Equation (15) is the stress tensor derived by Onuki [8], where the last term is the correction to the pressure tensor making the interfacial force act adiabatically. The coefficient κ from the free energy formulation is assumed here to be constant in both density and temperature. Through a constant κ the VdW theory predicts the interface tension of the fluid. A more detailed fit to more complex fluid data is beyond the scope of this work.

It is worthwhile to note here that, for test purposes, we have also implemented the formulation proposed by Anderson *et al.* [7]. Testing the two models against each other yielded practically indistinguishable results for a boiling simulation in a domain with a temperature gradient. It would be interesting to study in detail if any differences between these two models exist in a benchmark thermohydrodynamics case, but this is beyond the scope of the present work. However, our preliminary numerical tests indicate that the results of the two models are nearly identical and that the results presented here do not depend on the choice between these two models.

A. Boundary conditions

In addition to bulk dynamics boundary conditions for the thermodynamic variables need to be prescribed for studies of

different physical phenomena. In addition to assigning values for the temperature and velocity at solid walls, we need an open boundary allowing a flow of mass in and out. For instance, in a liquid-gas system fully enclosed by walls, two stable coexistence phases can appear after domain decomposition. Carefully engineering the initial condition in a wall-enclosed system can make the decomposition mimic the dynamics of phase change under constant pressure, but it is difficult to say *a priori* how well. Also a boundary condition for the contact line, here imposed via the density variable, is required to adequately describe boiling phenomena near a hot wall.

A solid wall has a different surface tension when in contact with liquid or gas. We denote these by σ_{sl} and σ_{sg} respectively, where the subscript l denotes liquid, s solid, and g gas. Together with the liquid-gas (σ) interface tension these give the equilibrium contact angle Θ_e described by Young's equation

$$\cos(\Theta_e) = \frac{\sigma_{sg} - \sigma_{sl}}{\sigma}. \tag{16}$$

In addition to the wetting boundary condition on the wall we prescribe a no-slip velocity, constant temperature (or a fully insulating wall), and no normal forces.

We follow the methodology by Jacqmin [16] and add a surface contribution to the free energy at the wall:

$$F = \int_V dx \left[f(\rho(x), T(x)) + \frac{\kappa}{2} |\nabla \rho(x)|^2 \right] + \int_S dS [\sigma_{sg} + (\sigma_{sl} - \sigma_{sg}) g(\rho, T)]. \tag{17}$$

In the same spirit as the isothermal Cahn-Hilliard model, we represent $g(\rho, T)$ as a polynomial that gives the values $g(\rho_g(T), T) = 0$ and $g(\rho_l(T), T) = 1$ for the coexistence densities of gas and liquid at a given temperature. We also require g to have a minimum and maximum in ρ at the gas and liquid densities [i.e., $\partial_\rho g(\rho, T)|_{\rho=\rho_{g/l}} = 0$]. This ensures that the boundary condition does not generate any artificial contribution to the $(\delta F/\delta \rho)$ for any of the coexistence densities at the wall. Furthermore, we assume local equilibrium at the wall, implying that the contact angle will immediately relax to its equilibrium angle. The wetting boundary condition here reads

$$\nabla_n \rho = \frac{\sigma \cos \Theta}{\kappa} \partial_\rho g(\rho, T), \tag{18}$$

where ∇_n is the normal gradient. This boundary condition is well defined on a wall with constant temperature, where a third-order polynomial describes g in analogy to the case of the Cahn-Hilliard free energy [28]. This makes the variation in g with respect to density to take the form of a regularized delta pulse, which is only nonzero in the interfacial region. Since no simple analytic expression exists for gas and liquid densities as a function of temperature for the VdW model, extending this to a wall with varying temperature is complicated.

For the open boundary condition of constant temperature and bulk pressure we propose to use vanishing normal gradients of the velocity fields, and constant density, temperature, and (bulk) pressure. The equation of state must be fulfilled by the values we impose to the latter three, meaning that the density at the open boundary must be either the gas or liquid density at the given temperature and pressure. Note that one

of these phases is in general stable and the other is metastable, unless the wall temperature and pressure is set exactly at the boiling point.

To summarize our boundary conditions, we have for the solid wall

$$v_i = 0, \quad \text{for every } i, \tag{19}$$

$$\nabla_n \rho = \frac{\sigma \cos \Theta}{\kappa} \partial_\rho g_T(\rho), \quad \nabla_n \rho = 0, \tag{20}$$

$$T = T_{\text{wall}}, \quad \nabla_n T = 0, \tag{21}$$

$$\nabla_n P_{ij} = 0. \tag{22}$$

Here the density and temperature conditions on the left-hand side are for a constant-temperature wall, and the right-hand side is for a fully insulating wall. The no-slip and zero-pressure gradient conditions apply for both cases.

The open boundary of a bulk fluid is given by

$$\nabla_n v_i = 0, \quad \text{for every } i, \tag{23}$$

$$\rho = \rho_{\text{wall}}, \tag{24}$$

$$T = T_{\text{wall}}, \tag{25}$$

$$P_{ij} = p_{\text{wall}} \delta_{ij}, \tag{26}$$

where for physical consistency it must hold that $p(\rho_{\text{wall}}, T_{\text{wall}}) = p_{\text{wall}}$.

III. NUMERICAL METHODOLOGY

The numerical simulations were carried out using the finite element toolbox FEMLEGO [25]. FEMLEGO is a symbolic tool that defines the differential equations, boundary conditions, initial conditions, and the method of solving each equation in a single MAPLE worksheet. It also inherits adaptive mesh refinement capabilities [26], which are used in these simulations. This enables us to have a high resolution of the interface without spending excessive computational time. The implementation of the mesh adaptivity can be described as follows: At each mesh refinement step an element is marked for refinement if the element size is still larger than the minimum mesh size allowed, and it does not meet a prescribed error criterion. In the case that an element meets the error criterion, it is marked for derefinement unless it is an original element. At the next refinement step, elements containing hanging nodes are marked for refinement. The refinement or derefinement stops if and only if no element is marked for refinement or de-refinement (see [26]). All variables are discretized in space using piecewise linear functions. A modified version of the characterized-splitting-based scheme [24], originally developed for single-phase compressible flow, is developed and tailored for the VdW phase change simulations. Details concerning the numerical scheme are presented in Appendix A.

A. Dimensionless units

The governing equations have been solved in dimensionless form. Since the dimensions of the systems in this study are at microscopic scales (i.e., $<1 \, \mu$m), gravitational effects can be neglected. The equations are scaled in such a way that the

fluid's critical properties are all of size unity. This means the equation of state (2) is turned into

$$\tilde{p}(\tilde{\rho},\tilde{T}) = \frac{8\tilde{T}\tilde{\rho}}{3-\tilde{\rho}} - 3\tilde{\rho}^2, \tag{27}$$

where the tilde denotes dimensionless variables. The corresponding dimensionless internal energy is

$$\tilde{e}(\tilde{\rho},\tilde{T}) = 4\tilde{T}\tilde{\rho} - 3\rho^2. \tag{28}$$

In dimensionless units the critical point is at $\tilde{T}_c = \tilde{\rho}_c = \tilde{p}_c = 1$. This gives us three equations that set our three physical dimensions of distance, time, and mass. Note that in physical dimensions the critical temperature is determined by the energy scale through the Boltzmann constant k_B. This is achieved by scaling the density and temperature by

$$\rho = \frac{m_p}{3b}\tilde{\rho}, \tag{29}$$

$$k_b T = \frac{8a}{27b}\tilde{T}, \tag{30}$$

and by $27b^2/a = x_0 t_0^2/m_0$. This leads to the following scaling of length (x_0), mass (m_0), and time (t_0):

$$x_0 = 2b^{1/3}, \tag{31}$$

$$m_0 = \frac{8}{3}m_p, \tag{32}$$

$$t_0 = 6b^{5/6}\sqrt{\frac{m_p}{a}}. \tag{33}$$

The gradient energy coefficient κ is related to the surface tension coefficient through Eq. (5), which is the experimentally measurable quantity to which we can fit our model. The kinematic viscosity (η_0) and heat conductivity (α_0) per density scale by their physical units. This leads to the three free variables that determine our VdW system:

$$\tilde{\eta}_0 = \frac{t_0}{x_0^2}\eta_0, \tag{34}$$

$$\tilde{\alpha}_0 = \frac{m_0 t_0}{x_0^2 k_b}\alpha_0, \tag{35}$$

$$\tilde{\kappa} = \frac{t_0^4 \sigma^2}{2m_0^2\left[\int_{\tilde{\rho}_g}^{\tilde{\rho}_l} d\tilde{\rho}\sqrt{\Delta\tilde{f}(\tilde{\rho})}\right]}. \tag{36}$$

One should note that the model predicts all the properties of the fluid once these three constants are set. This is, however, not enough to quantitatively model a real two-phase fluid, but the essential physical phenomena are captured with these parameters.

In the numerical simulations we choose the three parameters above based on material properties similar to those of water. The dimensionless units are determined from the critical properties of water: $T_c = 647$ K, $p_c = 22.1$ MPa, $\rho_c = 322$ kg/m^3, with the characteristic length $x_0 = 0.74$ nm, time $t_0 = 2.8$ ps, and mass $m_0 = 1.3 \times 10^{-25}$ kg. Note that

the characteristic length scale is similar to the interface width and not the bubble size in the simulations. Choosing the dimensionless coefficients

$$\tilde{\eta}_0 = 1, \tag{37}$$

$$\tilde{\alpha}_0 = 30, \tag{38}$$

$$\tilde{\kappa} = 1, \tag{39}$$

leads to the following dimensional properties for our VdW fluid at $0.5T_c$: kinematic viscosity $\eta_0 = 2 \times 10^{-7}$ m^2/s, heat conductivity per density $\alpha_0 = 6 \times 10^{-4} \frac{\text{J m}^2}{\text{kg K s}}$, and surface tension $\sigma = 0.07$ N/m. The lambda value for the liquid is then $\lambda_l = 0.7\frac{\text{W}}{\text{K m}}$.

IV. MODEL VERIFICATION AT ISOTHERMAL CONDITIONS

To verify our proposed model and the numerical scheme we study isothermal systems of a single vapor bubble immersed in its liquid at coexistence. At constant temperature we have coexistence with well-defined values for the gas and liquid densities. This allows us to numerically measure the surface tension via the Laplace pressure. We also use this as a measure of the accuracy of the numerical scheme. For simulations with an open boundary the pressure is fixed and allows us to observe the effect of surface tension on the metastability of the gas bubble and the liquid surrounding it. We extract from simulations the threshold for the critical bubble size that will either shrink or grow when placed in a superheated liquid. This critical bubble size is compared against the theoretical estimate. Finally, we verify the wetting boundary condition by measuring the contact angles from simulations after reaching steady state. The initial condition for the interface is far from its equilibrium shape and thus the interface undergoes significant evolution before reaching equilibrium.

A. Young-Laplace law

Since the coexistence values for gas and liquid densities at a given temperature for the VdW fluid can be calculated and the form of the Helmholtz free energy is known, the surface tension σ can be computed from Eq. (5) [18]. The interface tension causes a pressure increase in a circular domain of radius r compared to the surroundings. This pressure difference is given by the Young-Laplace law, which in 2D is given by

$$\Delta p = \frac{\sigma}{r}. \tag{40}$$

We compute the numerical steady state of a bubble in coexistence with a liquid in a closed system (i.e., one where all edges of a square 2D computational domain are solid walls). Initially a bubble is placed at the center of the domain surrounded by the liquid phase. Both the densities of the gas and liquid are at the coexistence density, and we set the initial interface profile to interpolate between these using a tanh function. Even though small spurious velocity currents persist at the interface after reaching what we interpret as the numerical steady state, the bulk values for both liquid and gas are constant to the fifth decimal. These density values tell us how well our numerical simulation reproduce the VdW coexistence and by using the equation of state (27) we obtain the pressure inside
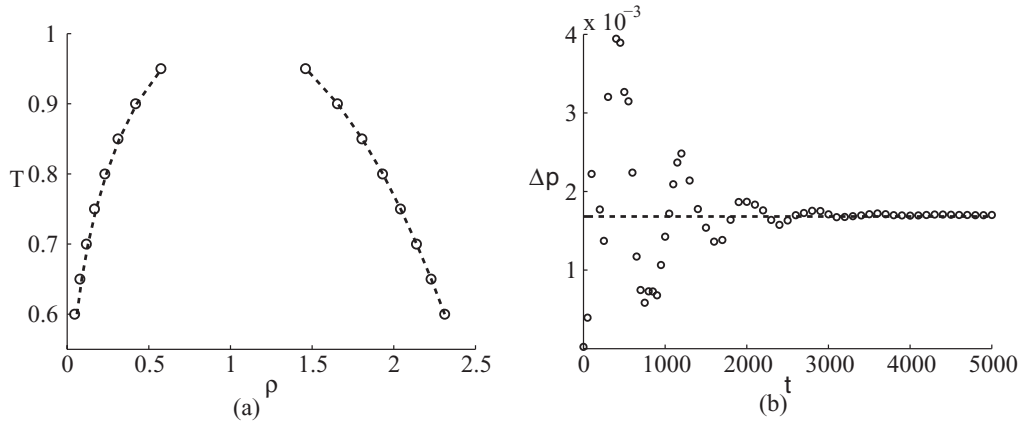
FIG. 2. (a) Numerical coexistence densities denoted by hollow markers plotted against the analytical VdW coexistence lines (dashed lines). Uncertainty due to Laplace pressure caused by inaccuracy in the numerical densities are all within the marker size. (b) Time series of the pressure difference inside and outside the gas bubble. The dashed line is the analytical Laplace pressure.

and outside the bubble. The difference in these pressure values gives a numerical value for the interface tension via Eq. (40).

We study the Laplace pressure for isothermal coexistence at eight different temperatures between $T = 0.95$ and $T = 0.6$ and for five different bubble sizes between $50 \leqslant r \leqslant 150$. The width of the diffuse interface depends on temperature, but stays well within the range of 1 to 10, ensuring that there is still a length-scale separation between the bubble size and the interface width. At temperatures below $T < 0.6$, or density contrast beyond $\rho_l/\rho_g > 50$ our numerical results become inaccurate. In Fig. 2(a) we compare the numerical density coexistence values against the analytical prediction for different temperatures. For each temperature we plot the largest and smallest density values taking into account the predicted Laplace pressure. Thus the smallest bulk density of the gas is the smallest value observed minus the Laplace pressure. Since in a finite system the Laplace pressure could also manifest itself as decreased pressure in the liquid domain, the largest bulk density of the liquid is the largest value observed plus the

Laplace pressure. As seen from Fig. 2, the largest and smallest value overlap in most cases and agree well with the VdW result. Some differences are observable at low temperatures in the gas branch due to the large compressibility of the gas.

In Fig. 2(b), we show a time series of the pressure difference inside and outside the bubble as it approaches equilibrium. The system is here at $T = 0.95$ and the bubble has a radius of $r = 75$. As an initial condition we prescribe coexistence values with the same pressure. As the bubble equilibrates, sound waves are produced that propagate across the simulation domain. When the density profile has stabilized with only very minor variations, we measure the pressure difference between the gas and liquid phases.

The gas-liquid interface tension provides a sensitive check of the accuracy of the solution method, since changes in density due to Laplace pressure are typically in the third decimal in the density. This means only fractions of a percent on the liquid side and a few percent on the gas side. By observing densities of the gas and liquid domains we obtain the interface
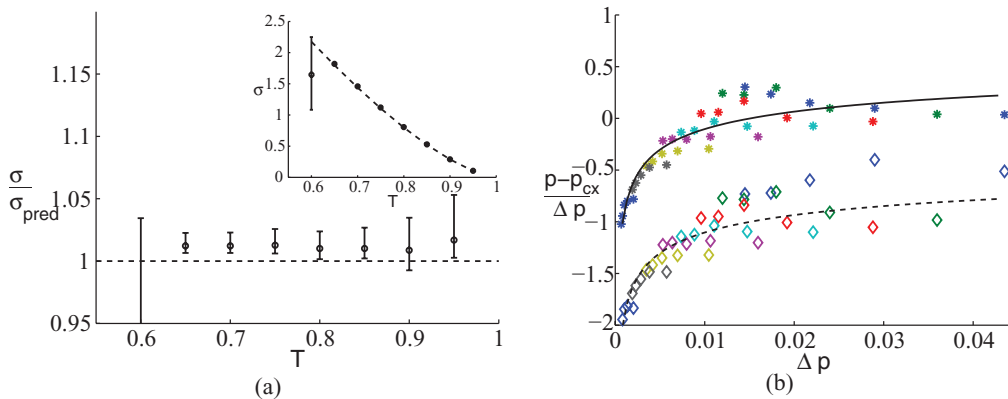

FIG. 3. (Color online) (a) Numerically measured surface tension of bubbles with different sizes for eight temperatures at isothermal conditions. The surface tension is measured by extracting the pressure difference between the gas and liquid domains, which is scaled with the predicted values from Eq. (5). At temperatures above $T = 0.65$ we observe interface tensions within 5% of the prediction. The inset shows the unscaled data, where the dashed line is the theoretical value. (b) Data for the pressure difference, where the gas data are denoted by stars and the liquid data as diamonds. The solid line is a fit to the gas data and intended as a guide to the eye. The dashed line is a shift by unity in the y axis that is equivalent to the Laplace pressure. This dataset shows that Laplace pressure difference between the gas and liquid sides is well characterized numerically and obtained to a much higher degree of accuracy than the coexistence pressure in the bulk phases.

tension data shown in Fig. 3(a). The results agree with the interface tension values predicted by Eq. (5) to an accuracy of about 5%. Our numerical accuracy for the surface tension is in the same range as presented in the recent study by Pecenko *et al.* [18]; however, they evaluated the numerical error in a different manner. The error bars show the smallest and largest values we obtain for the surface tension using different bubble sizes at the same temperature.

Observations at temperature $T = 0.6T_c$ show that our simulations become inaccurate when we decrease the temperature further from T_c than this. The density contrast increases the further the temperature is from the critical temperature, which makes the problem harder to solve numerically. Another aspect is that the equations have a singularity at zero density, which adds another numerical complication. At lower temperatures the interface thickness reduces significantly, requiring also a much finer grid resolution. Exploring these different effects is, however, beyond the scope of the current study and we note that the range of validity where we verify our method ($T > 0.7$) compares favorably with earlier studies [8,17,19]. One reason for this is the adaptive mesh refinement employed on our work, which makes it computationally easier to resolve the interface as it becomes thinner and thinner as temperature is quenched deeper below the critical point.

In Fig. 3(b) we show the data for the pressure difference in the gas and liquid sides as a function of the predicted pressure difference from Eqs. (5) and (40). The simple picture of Laplace pressure is to have the coexistence pressure in the external liquid domain and the coexistence pressure plus the Laplace pressure in the internal gas domain. This would correspond to stars at 1 and diamonds at 0 in the plot. Figure 3(b) shows that, surprisingly, the Laplace pressure is recovered by our method better than the coexistence pressure itself. That is, the pressure difference between the bubble and liquid bulk is obtained to a much higher degree of accuracy than the coexistence bulk pressure itself. Nevertheless, the VdW bulk density values are reproduced to within a few percent for the gas and a fraction of a percent for the liquid. The unexpected result is that we consistently observe Laplace pressure differences corresponding to density differences less than the accuracy of the coexistence densities.

B. Growing or shrinking of a bubble

To verify our open boundary condition in Eqs. (23)–(26) we study an isothermal system in a square 2D domain with three physical walls and one open boundary with a fixed pressure. If the pressure is slightly below the coexistence value for the given temperature, the gas phase is stable and the liquid is metastable. An initial condition set as a gas bubble immersed in the metastable liquid will then force the gas bubble either to grow or shrink depending on the initial size of the bubble.

Referring to the details in Appendix B, we predict the critical radius of the bubble that will neither grow nor shrink in 2D to be

$$r_{\text{crit}}^{\text{pred}} = -\frac{\sigma}{2}\left\{[f(\rho_g, T) - f(\rho_{\text{ext}}, T)]\right.$$

$$\left. + \frac{\rho_{\text{ext}} - \rho_g}{\rho_l - \rho_{\text{ext}}}[f(\rho_l, T) - f(\rho_{\text{ext}}, T)]\right\}. \quad (41)$$
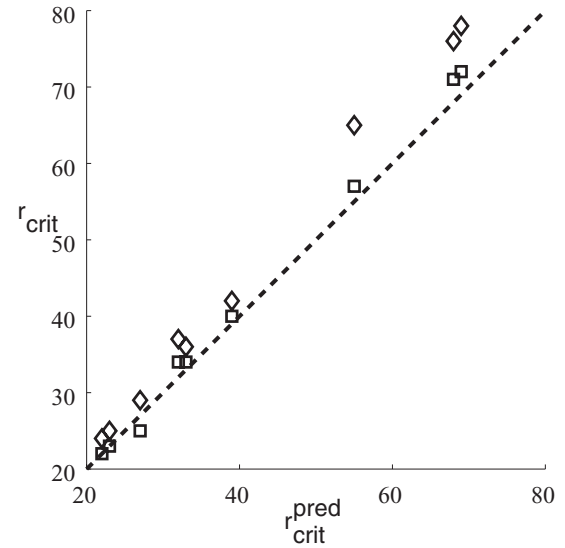

FIG. 4. Numerically measured critical bubble radius of a bubble in a superheated liquid plotted against the prediction from Eq. (41), here represented by the dashed line. Stars are lower bound observations and diamonds are upper bound observations.

In order to determine whether the bubbles grow or shrink, we start with an initial condition that is close to the theoretical estimate. Exactly at the threshold for the critical bubble radius acoustic waves and spurious velocity currents might trigger the bubble to either grow or shrink. As this threshold is approached we notice that the mass fluxes become increasingly slow, resulting in an unfeasible simulation time to determine whether the bubble shrinks or grows. Instead, we successively increase and decrease the bubble size to a point where shrinking or growing is well defined in the simulations. This gives us upper and lower bounds for the critical bubble size.

In Fig. 4 we show the numerically obtained upper and lower bounds for the critical bubble radius. The markers denote the numerical result, diamonds illustrate the upper bound, and squares show the lower bound. The dashed line shows the analytical prediction from Eq. (23). Simulations were preformed at three different temperatures, and three different superheats. At temperature $T = 0.8$ with the coexistence pressure $p_{\text{coex}} = 0.383$, we use external pressures $p = \{0.37, 0.36, 0.35\}$; at $T = 0.85$, $p_{\text{coex}} = 0.504$, and $p = \{0.495, 0.485, 0.475\}$; and at $T = 0.9$, $p_{\text{coex}} = 0.647$, and $p = \{0.64, 0.635, 0.63\}$. We note that our method captures the critical bubble sizes well, considering the sensitivity of the test, but the numerical values are consistently about 5% to 10% higher than what we predict. As Appendix B shows, the estimate is also approximate since, numerically, the pressure in the metastable liquid varies smoothly between the coexistence and external pressures.

C. Wetting contact angle

In addition to the open boundary condition there is also another crucial ingredient needed to model boiling; namely the boundary condition for the contact line. The contact line is the point where the three phases meet. We adopt here a methodology similar to what has been commonly employed
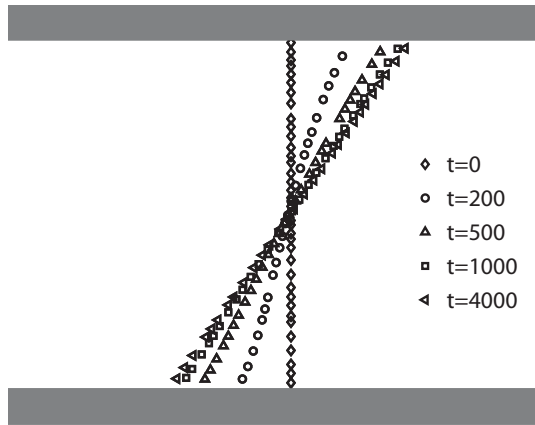
FIG. 5. Interface evolution of an initially straight interface that spreads on two walls until it finds its equilibrium shape. The temperature of the system is $T = 0.8T_c$. The lower wall has an equilibrium angle $\Theta_e = 60°$ and the upper wall has $\Theta_e = 120°$.

for the isothermal Cahn-Hilliard method [16], and for now assume that the temperature at the boundary is fixed. This implies that we can *a priori* determine the coexistence densities for gas and liquid. The wetting boundary condition is obtained from Eq. (18) and it appears by taking the variation of the free energy with respect to density.

In Eq. (18), $g_T(\rho)$ is an interpolating function between the two stable phases acting as a switch between having a dry or wet solid. It is convenient to use higher-order polynomials for $g_T(\rho)$, where we require that, at the coexistence, densities $g_T(\rho_l) = 1$ and $g_T(\rho_g) = 0$. In addition, we require that the variation of $\partial_\rho g_T(\rho) = 0$ for $\rho = \rho_l$ and $\rho = \rho_g$, making the boundary condition to be effective only at the interface area. Often a third-order polynomial is used since it fulfills these requirements. The third-order polynomial is exact in the case of the Ginzburg-Landau free energy. For the VdW, the third-order polynomial is an approximation. Note that a constant temperature at the wall is needed to set g as above.

As a verification to the wetting boundary condition we measure the apparent contact angle after the solution has reached equilibrium. The simulation setup is as follows: A rectangular domain with constant temperature is applied, where the domain is separated in the middle with a straight interface with gas on the left and liquid on the right side of the interface. The upper wall has an equilibrium angle of $\pi - \Theta_e$ and the lower wall has an angle Θ_e, which makes the interface a straight line in the steady state. We define the contact angle on the liquid side of the interface. The interface goes through nontrivial relaxation dynamics before reaching equilibrium. In Fig. 5 we show the initial condition and the interface shape as four snapshots in time. Initially the contact line moves rapidly over the solid walls due to the capillary force generated at the wetting foot region of the contact line. As the interface approaches its equilibrium shape, the interface motion decelerates. Finally, the interface finds its equilibrium shape as seen in Fig. 5.

We evaluate the numerical prediction based on the boundary conditions (19)–(22) for the contact angle for three different temperatures and for several surface wettabilities [see Fig. 6(a)]. The contact angle is measured along the density contour $(\rho_g + \rho_l)/2$, where the angle is defined between the straight line along the interface and the wall on the liquid side. We notice in Fig. 6(a) that the deviation between the numerically measured contact angle and the imposed angle is within about three degrees. The deviation seems to be slightly dependent on the equilibrium angle, which might imply that our method for extracting the angle could be refined. Overall, we find the results in good agreement with expected values. It should be noted that the constants appearing in the third-order polynomial $g_T(\rho)$ are adjusted according to the coexistence densities at the respective temperatures and that the change in temperature did not influence the results significantly.

Figure 6(b) shows the evolution of the apparent contact angle Θ for an equilibrium angle $\Theta_e = 60°$ at $T = 0.9$, where $\Theta - \Theta_e$ is plotted on the y axis. Initially the interface is perpendicular to the wall and it quickly approaches the imposed value, where it eventually takes a steady-state value
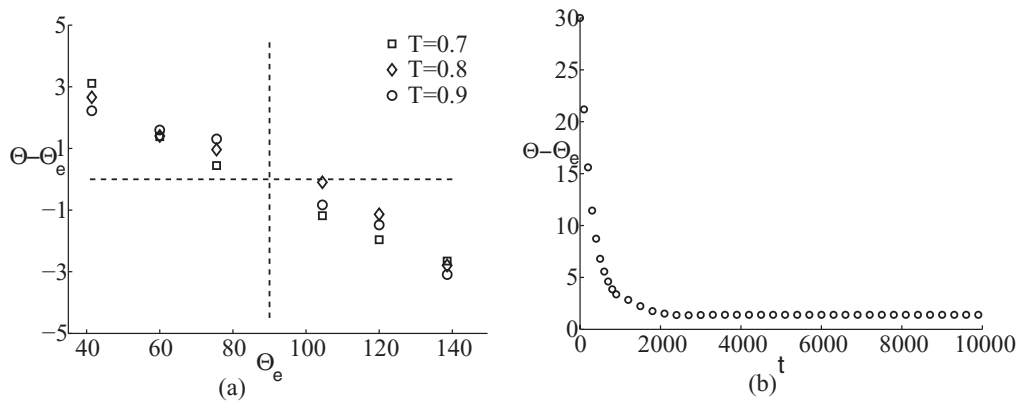

FIG. 6. Contact angle measured in the system with a straight interface, see Fig. 5. (a) Measured difference of the contact angle at numerical equilibrium and the imposed one as a function of the set contact angle in degrees. Six different Θ_e values were measured at three temperatures each. Note that the numerical contact angle is a few degrees toward the perpendicular compared to what it is set. (b) Time series of the contact angle as measured along the isocontour for the density $(\rho_g + \rho_l)/2$ where it meets the top and bottom walls. The initial condition at perpendicular contact relaxes quickly and obtains a value about two degrees toward the perpendicular compared to what we theoretically impose.

with a difference in angle of $<2°$. By comparing the numerical results in Fig. 6 to the Laplace test in Fig. 2, we notice that any oscillations from acoustic waves are not significantly influencing the results seen in Fig. 6. Acoustic waves are also present in the simulations presented in Fig. 6, but they give a very small contribution compared to the flow generated by the spreading motion.

V. DYNAMICS OF BOILING

We numerically investigate a bubble near a hot (de)wetting wall in a closed and an open system. The computational domain is again a 2D square. The lower boundary is the hot wall and has constant temperature. The boundaries to the left and right are insulated walls with an equilibrium angle $\Theta_e = 90°$, where all walls are imposed with a no-slip condition for the velocity. A temperature gradient is imposed between the upper and lower boundaries corresponding to a heated system. The density of the liquid phase changes from top to bottom as a function of the initial temperature profile such that the pressure in the liquid is constant. A coexistence gas bubble is initiated close to the wall to mimic the first nucleate. This bubble is at first not in direct contact with the wall, but slowly drifts toward the hot wall by the unbalanced surface tension at its front and rear, thus generating a type of Marangoni flow. A hyperbolic tangent interpolation is used to set initial interface width close to the predicted numerical solution. In the closed system this bubble has a radius $r = 50$ that is slightly larger than for the open system. The reason for this choice is that the mass fractions of gas and liquid phases in the closed system remain constant and we want to study the evolution of a larger

bubble. In the open system the initial bubble radius is $r = 30$, but the bubble grows similar to a boiling process contrary to the closed system.

The objective is to first observe the difference between the closed and the open systems emphasizing the role of the constant pressure boundary in describing the physics of boiling. Then we verify that we obtain both film and nucleate boiling as functions of the wettability of the hot wall. We show simulations with two different equilibrium angles $\Theta_e = 45°$ and $\Theta_e = 177°$. On the upper wall the temperature is $T = 0.88$ and the lower hotter wall is at a temperature $T = 0.9$. The pressure at the open boundary is set to correspond to the boiling temperature of $T = 0.89$.

Figure 7 shows the simulation result for the spreading in a closed system with a thermal gradient as the bubble comes in contact with the lower wall, which has an equilibrium angle of $\Theta_e = 177°$. The wall favors the gas phase and the bubble starts to spread rapidly along the wall. The temperature decreases at the foot region of the bubble, where it has the smallest radius of curvature, as shown in Fig. 7(a). In this region the mass flux is also the greatest; see Fig. 7(d). As the bubble continues to spread, the temperature inside the bubble becomes more and more uniform, as shown in Fig. 7(b). Figure 7(e) shows two vortices are generated, showing the evaporation close to the contact line and the condensation at the top of the bubble.

Later in time the bubble has almost spread across the domain and formed a gas film at the hot solid surface; see Fig. 7(c). As shown in Fig. 7(e) two evaporation-condensation vortices persist in the steady state. The vortices resemble Rayleigh-Bénard convection rolls, but they are created by the
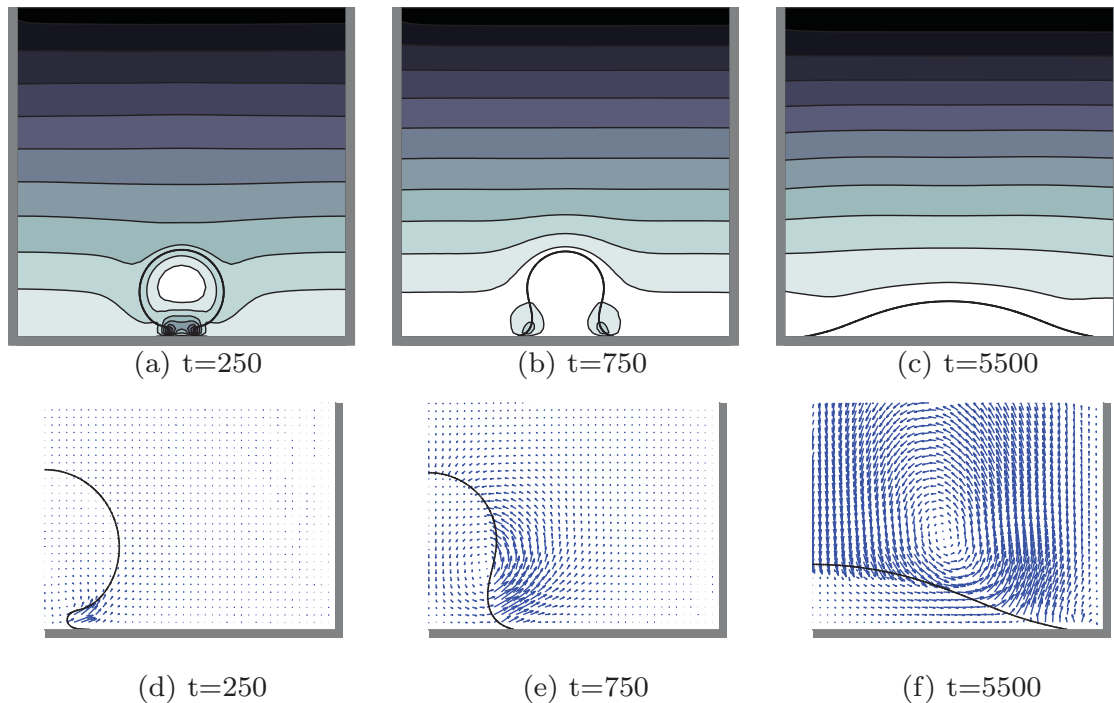

| (a) t=250 | (b) t=750 | (c) t=5500 |

| (d) t=250 | (e) t=750 | (f) t=5500 |

FIG. 7. (Color online) Closed system with $\Theta_e = 177°$ on the hot wall where the interface is illustrated by the contour line drawn at the mean between the liquid and gas coexistence densities $\rho = (\rho_l + \rho_g)/2$. Panels (a), (b), and (c) show the temperature profile with equidistant isotherms between $T = 0.9$ and $T = 0.88$. Panels (d), (e), and (f) show mass flux vectors on the right-hand side of the vertical symmetry axis at the middle of the system.
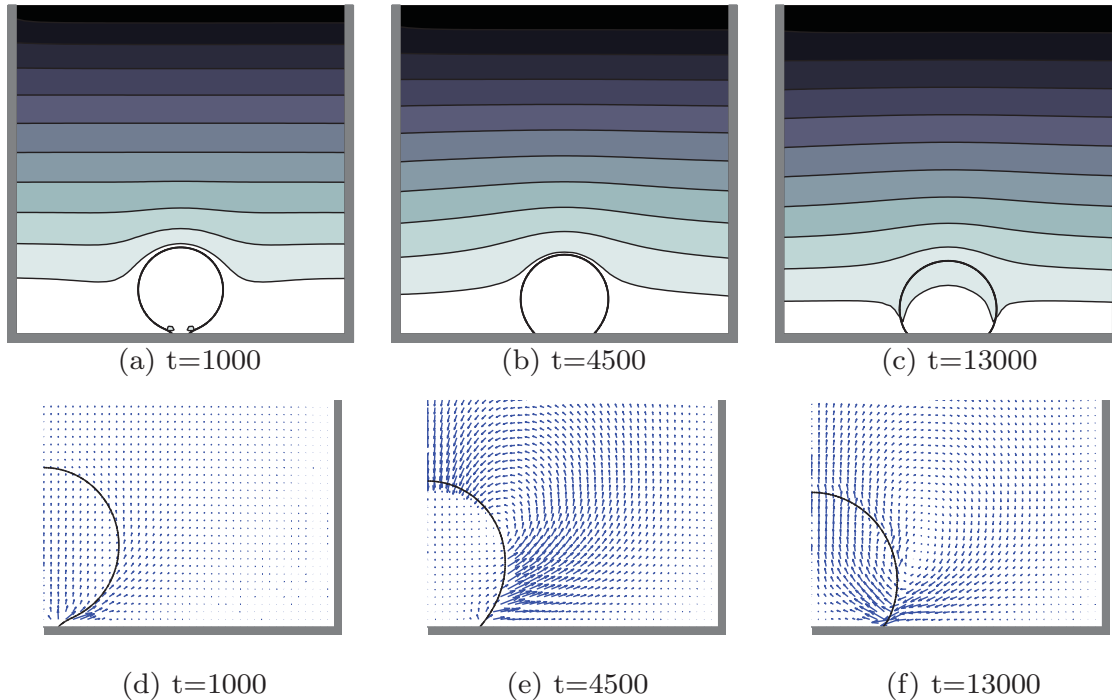
(a) t=1000

(b) t=4500

(c) t=13000

(d) t=1000

(e) t=4500

(f) t=13000

FIG. 8. (Color online) Closed system with $\Theta_e = 45°$ on the hot wall where the interface is illustrated by the contour line drawn at the mean between the liquid and gas coexistence densities $\rho = (\rho_l + \rho_g)/2$. Panels (a), (b), and (c) show temperature profiles with equidistant isotherms between $T = 0.9$ and $T = 0.88$. Panels (d), (e), and (f) show mass flux vectors on the right-hand side of the vertical symmetry axis in the middle of the system.

two-phase structure and temperature gradient—no gravity is present here.

By making the lower wall more attracted to the liquid phase, the dynamics observed in the simulations change (see Fig. 8). The lower wall here has an equilibrium contact angle of $\Theta_e = 45°$ and all other parameters are the same as presented in Fig. 7. The bubble spreads here in a much slower fashion, but the same evaporation to condensation flow is observed, [see Figs. 8(b) and 8(d)]. At the final stage of the spreading and close to steady state the mass flux at the contact line changes direction as shown in Figs. 7(c) and 7(e). Two vortices are present in the steady state as for the case of the hydrophobic wall in Fig. 7, but the vortices are in the opposite direction. A similar system was experimentally investigated by Nikolayev *et al.* [6]. However, the length scales of observation of their cryogenic hydrogen experiment are larger by orders of magnitude than our current numerical system, making direct comparison impossible.

We note that the bubble evolution in the closed system as shown in Figs. 7 and 8 strongly resembles an isothermal spreading event, and that the mass fraction with gas seems fairly constant. The observed dynamics is also consistent with observations made by Ref. [8] for a similar VdW system.

In Figs. 9 and 10 we show the cases equivalent to those of Figs. 7 and 8, with the important difference that we now have the constant pressure boundary condition at the top. This allows mass flux in and out of the domain and thus this corresponds to boiling at a constant pressure.

Figure 9 shows boiling at a wall with an equilibrium angle $\Theta_e = 177°$. As the gas bubble comes in contact with the hot solid wall the temperature profile and the mass flux,

shown in Figs. 9(a) and 9(d), are indeed similar to those in the corresponding closed system. But as the bubble starts to spread, a rapid mass transfer from liquid to gas takes place and leads quickly to the formation of a thin gas film on the hot wall, see Figs. 9(b) and 9(c). At time $t = 2000$ the surface is entirely covered by gas and, in analogy to the dryout process, a sharp temperature gradient is created as the gas insulates the hot wall from the interface where boiling occurs [3]. After the interface comes in contact with the insulated walls at the two sides of the domain, the rate of phase change decreases rapidly, corresponding to film boiling. Notice that the interface has a nearly constant temperature at its boiling point $T = 0.89$ [see Fig. 9(e)] and a linear temperature profile in accordance to Fourier's law while a drastically higher temperature gradient in the gas than in the liquid is about to be established.

By making the hot boiling surface more hydrophilic, the qualitative features of boiling dynamics change dramatically (see Fig. 10). Initially, the bubble starts to wet the hot wall as shown in Figs. 10(a) and 10(c), although the phase change is much less than for the hydrophobic wall. The temperature takes a nearly linear profile inside the gas, where it is distorted close to the contact line, as shown in Fig. 10(b). The majority of the phase change takes place at the contact line. As the bubble evolves past the initial contact with the wall a steady boiling regime is established, characterized by a semicircular interface at a temperature close to the boiling point, as shown in Figs. 10(b) and 10(c). This boiling regime is characteristic of nucleate boiling, where the bubble would grow to orders of magnitude larger than our numerical system until gravity detaches it.
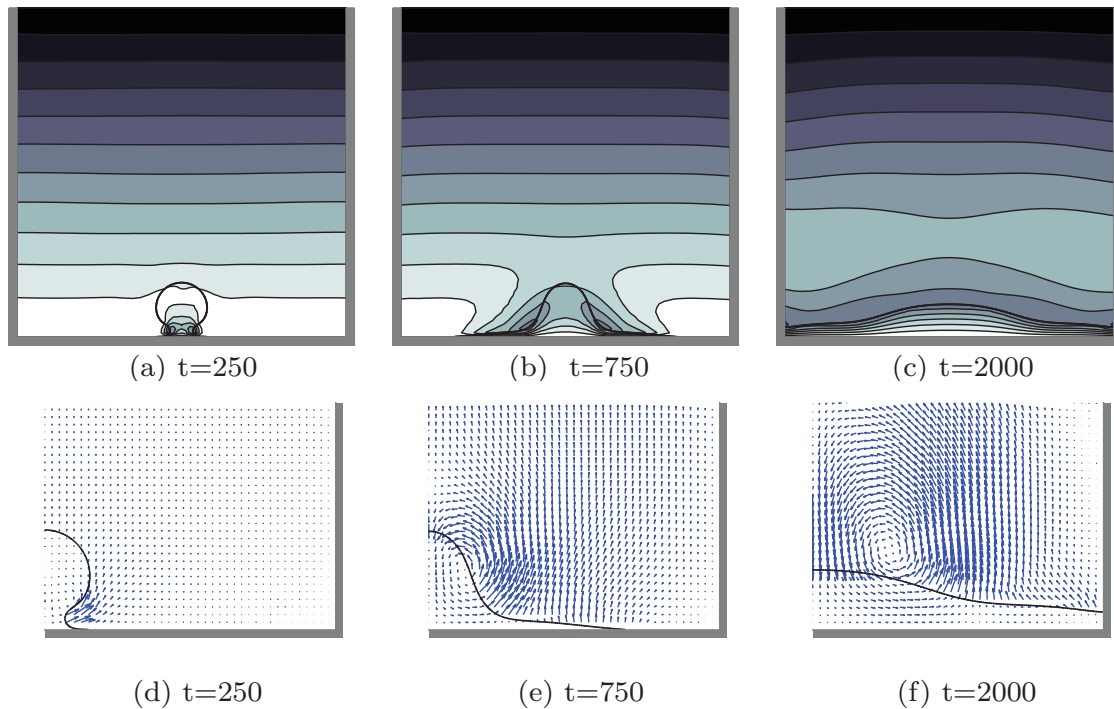
(a) t=250   (b) t=750   (c) t=2000

(d) t=250   (e) t=750   (f) t=2000

FIG. 9. (Color online) Open system with $\Theta_e = 177°$ on the hot wall where the interface is illustrated by the contour line drawn at the mean between the liquid and gas coexistence densities $\rho = (\rho_l + \rho_g)/2$. Panels (a), (b), and (c) show temperature profiles with equidistant isotherms between $T = 0.9$ and $T = 0.88$. Panels (d), (e), and (f) show mass flux vectors on the right-hand side of the vertical symmetry axis in the middle of the system.

The latent heat of boiling keeps the temperature at the gas-liquid interface close to the boiling point even when the interface reaches down to the hot wall at the contact line. This means that most of the thermal energy flowing into the fluid from the hot wall, and thus most of the boiling, happens at the contact line. Notice that there is a strong peak in mass flux going into
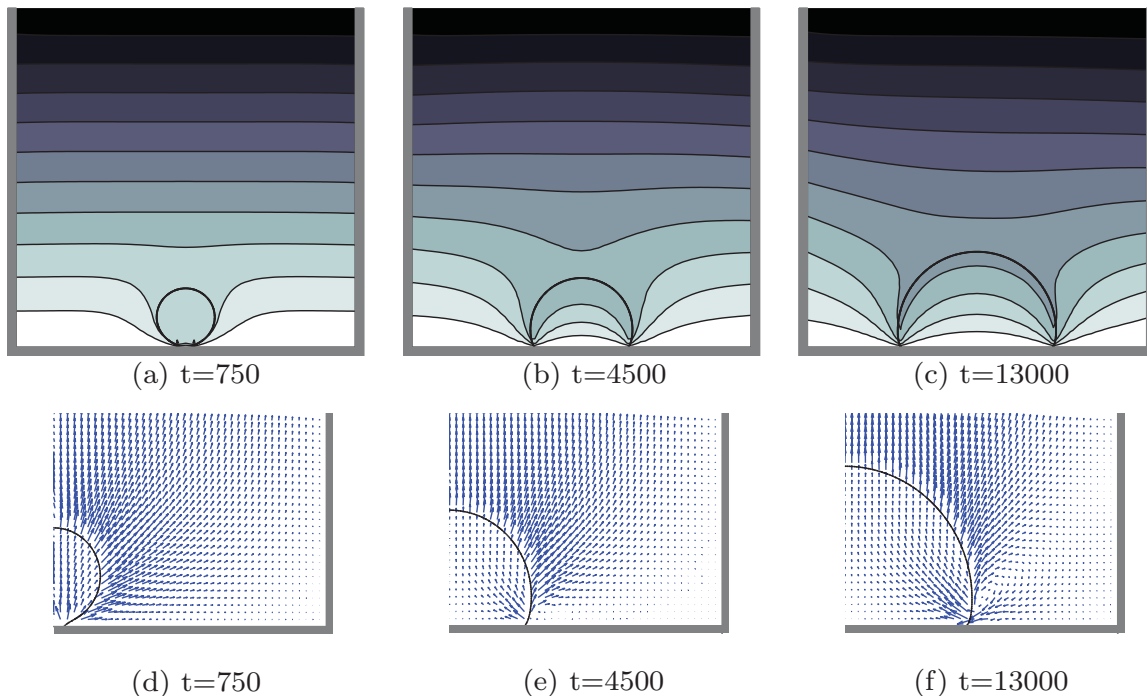

(a) t=750   (b) t=4500   (c) t=13000

(d) t=750   (e) t=4500   (f) t=13000

FIG. 10. (Color online) Open system with $\Theta_e = 45°$ on the hot wall where the interface is illustrated by the contour line drawn at mean between the liquid and gas coexistence densities $\rho = (\rho_l + \rho_g)/2$. Panels (a), (b), and (c) show temperature profiles with equidistant isotherms between $T = 0.9$ and $T = 0.88$. Panels (d), (e), and (f) show mass flux vectors on the right-hand side of the vertical symmetry axis in the middle of the system.

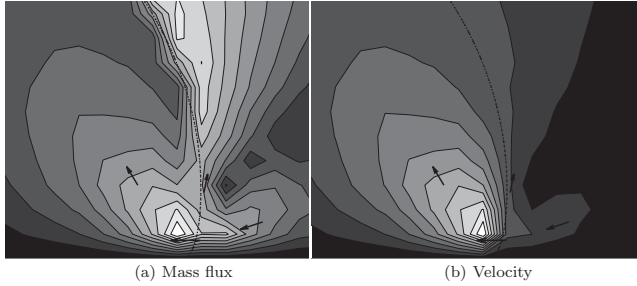(a) Mass flux   (b) Velocity

FIG. 11. Closer look at the contact line region of Fig. 10(f). The mass flux magnitude profile (a) and the velocity magnitude profile (b) are shown near the contact line in the steady nucleate boiling regime. The black line is the interface as in Fig. 10. The arrows are schematic guides to the eye of the direction of the flow. The flow is into the bubble at the foot and out of the bubble further away from the contact line. This prominent effect is interpreted as vapor recoil.

the bubble at the contact line in the steady-boiling regime. While average mass flux must be away from the growing bubble due to mass conservation, we observe the opposite at the contact line foot of the bubble, and a flow vortex is generated at the foot. This flow is consistent with the mechanism of vapor recoil and we interpret our results as verification that vapor recoil is present at the microscale flows of nucleate boiling and leads to an apparent contact angle that appears more hydrophobic than the microscopic equilibrium contact angle we impose.

The flow at the contact line in the steady nucleate boiling regime is shown in more detail in Fig. 11, where we plot the magnitudes of the mass flux and the velocity. A prominent jet into the bubble from the contact angle is seen in the velocity profile. The steep gradient in the mass flux at the contact line causes a force that distorts the interface leading to an apparent contact angle. The interface profile meets the boiling surface at the equilibrium contact angle if observed at the scale of the interface width, which is the smallest physical scale. This we have imposed via the wetting boundary condition. If the contact line is observed further away, distortion of the angle is seen clearly beyond what is expected due to the finite radius of the bubble. This is due to dynamical effects at the contact line in the steady nucleate boiling regime. Qualitatively the full thermal hydrodynamics are thus consistent with the vapor recoil picture [10]. Quantification of this effect is beyond the scope of this paper.

Figure 12 shows the time evolution of total mass in the four computational systems we considered here. m_0 is the initial mass of the system and $m(t) = \int \rho(t, x, y) dV$ is the mass at a given time. The closed systems are included to show that mass is indeed conserved. For the open systems the hydrophobic wall causes a rapid initial phase change as the gas spreads on the wall and film boiling sets on. The inefficiency of film boiling is apparent as a rapid decrease in the phase-change rate at later times. As the insulating gas layer grows, so does the insulation, and the boiling rate continuously decreases.

Figure 12 shows a linear boiling regime for the hydrophilic boiling surface. The linear rate is consistent with the boiling happening dominantly at the contact line point. Since the interface adjusts to the boiling temperature, the heat flux in the contact line region remains nearly constant in time as the
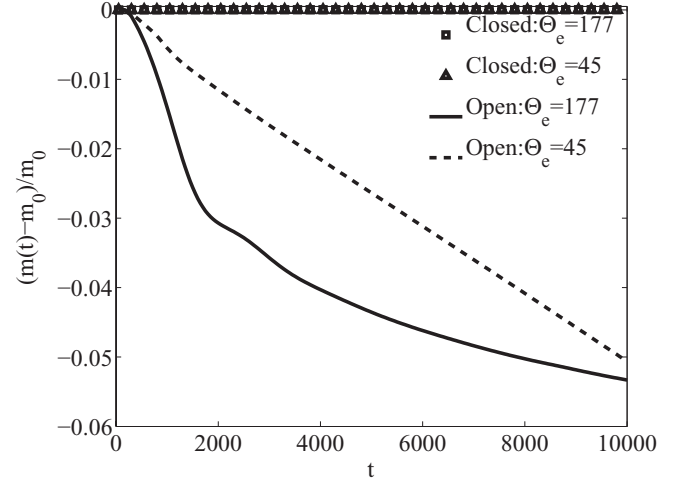

FIG. 12. Rate of mass change in systems with temperature gradients. Boiling is seen as change in total mass in the open systems.

contact line moves as the bubble grows. In fact, all the flow properties in the contact line region remain the same as the contact line advances in the steady-boiling regime.

VI. SUMMARY AND DISCUSSION

We have presented a numerical model for VdW fluids that enables study of boiling phenomena under constant, tunable external pressure and at a boiling surface of tunable wetting properties. The main development is here the implementation of an open boundary under constant external pressure that allows a flux of mass in and out of the domain. We propose also a boundary condition for the contact line, which lets us prescribe the equilibrium contact angle for the solid substrate.

The numerical scheme is based on a modification of the characteristic-based-splitting scheme, first developed for single-phase compressible flow by Ref. [24]. We verify our methodology by several isothermal validation cases. First, we study the Young-Laplace law of a static bubble submerged in its coexistence liquid. This allows us to measure the surface tension coefficient, where the results were found in to be good agreement with theory. Notice that the surface tension coefficient was reproduced with a similar level of accuracy as in the recent work [18].

An open boundary condition based on thermodynamics has been proposed to set a constant external pressure for the system, allowing mass flux into or out of the system. We verify this boundary condition by considering bubbles in metastable, superheated liquid. The Gibbs free energy yields an estimate for the limiting size of initial gas bubble that, absent fluctuations, will overcome the interface tension and grow toward the stable gas state as opposed to shrinking toward the metastable liquid state. We find our numerical test cases agreeing reasonably well with the estimate at different temperatures and superheats.

Contact lines and the solid-surface energy are believed to be important elements in a boiling process. It is therefore important to allow for modeling of solid walls with different equilibrium contact angles. A model for the wetting is proposed here for VdW fluids, which is based on the methodology

used in the isothermal Cahn-Hilliard modeling of wetting [16]. We verify in a numerical test case, where the initial interface shape is much different from the equilibrium shape, that we indeed capture the imposed equilibrium contact angle.

Using the VdW fluid as benchmark, parametrized to have properties of the correct order of magnitude compared to water across the coexistence region, we study a numerical system that we believe contains the relevant physics of boiling at the microscopic scales. Initially we seed the simulation with a bubble nucleate close to the hot wall. We study both the dynamics in a closed and open system with a thermal gradient. The results indicate that the open constant-pressure boundary brings out the physics instrumental to boiling, and we find both film and nucleate boiling regimes as function of surface wettability. In particular, the flow profile close the the three-phase contact line at the hot wall shows the vapor recoil mechanism [6,10,30] as it arises from the full thermal hydrodynamics. In the case of boiling on the hydrophobic solid we observed a gas layer that is rapidly formed and covers the hot surface and then acts to insulate the gas-liquid interface from the hot wall, drastically reducing the boiling rate.

While our model captures much of the boiling physics, limitations still exist in numerically simulating practical boiling as it happens in industrially relevant conditions and devices. First, no thermal fluctuations exist in the model and as such nucleation cannot be modeled. This means that the very initial stages of bubbles as they are formed cannot be predictively captured. Given that nucleation sites in heterogenous boiling are deterministically activated or deactivated as functions of superheat, the lack of nucleation in the model is not expected to be crucial. The more important question is whether a site remains active and emits a steady trail of bubbles by pinch-off once seeded, which the model could rather directly be applied to. Second, the diffuse interface methodology is also limited in how large systems can be studied, since the interface width, which must be numerically resolved, is limited to physical scales if physical surface tension is desired. This means that we cannot reach scales where bubble departure by pinch-off due to gravity happens or where coalescence of several bubbles is important. However, if the vapor recoil picture of dryout is correct, the transition happens at the microscale of single-bubble growth, and this regime can be reached by our numerical methodology whereas it is notoriously difficult by experiments.

Two crucial extensions for the methodology presented here are desirable, but beyond the scope of this paper. They represent the third and fourth limiting elements of the method. Unlike the physical scales, these should be relatively straightforward to address in future work. Third is extending the numerical solution of the model to cylindrical coordinates, as done in Ref. [17]. In cylindrical coordinates the numerical load is not much larger than here, but the boiling at the contact line is expected to be much better described. In particular, the extension of the length of the contact line as the bubble grows is crucial. As the contact line becomes longer the total heat transfer from the hot wall, and thus the boiling rate increases and so does the force of the interface tension attempting to keep the bubble spherical. Balance of these is expected to be crucial in how vapor recoil is suggested to cause dryout by single-bubble spreading. Fourth and finally, a hot wall of constant heat flux as opposed to constant

temperature would be interesting and useful, especially if finite heat conductivity along the wall could also be included. This calls for a significantly more complex boundary condition if wetting properties are also to be included, however.

Another interesting possibility for future studies is comparison with molecular dynamics simulations, which with modern computers should be feasible in the microscopic scales here considered. Recently, it was shown by Ref. [31] that molecular dynamics simulations capture the molecular scale density fluctuations in bulk phases of the square gradient energy model. We note that our contact angle boundary condition assumes local equilibrium by minimizing surface energy. As such it enforces the equilibrium contact angle at the smallest scale. The results we get appear reasonable, but detailed comparison with experiments might require a finite relaxation time toward equilibrium at the contact line following Ref. [32].

APPENDIX A: NUMERICAL SCHEME

We apply a modification of the characteristic-based split (CBS) method of Nithiarasu *et al.* [23,24] to solve the governing equations. In its original form the CBS method does not consider the energy equation as part of the flow solution; rather, it is treated as a passive scalar. We find that the latent heat strongly couples the energy and density equations and, thus, under certain circumstances, a significant improvement in numerical efficiency is obtained by treating the energy equation in the same manner as the density equation in the correction step of the CBS method.

Here we will present the method for Onuki's set of the Van der Waals–Navier-Stokes equations (12)–(15). The CBS time integration step from time step n to $n + 1$ starts with an explicit predictor mass flux U_i^* ($U_i = \rho v_i$) solved from the momentum equation

$$
\begin{aligned}
U_i^* = U_i^n + \Delta t &\left\{ -\partial_j \left(U_i^n v_j^n \right) + \partial_j \eta^n \left[\partial_i \left(\frac{U_j^*}{\rho^n} \right) + \partial_j \left(\frac{U_i^*}{\rho^n} \right) \right] \right\} \\
&+ \Delta t \left\{ F_i - \partial_j \left\{ \left[p - \kappa \left(\rho \partial_k \partial_k \rho + \frac{1}{2} \partial_k \rho \partial_k \rho \right) \right] \delta_{ij} \right. \right. \\
&\left. \left. + \kappa \partial_i \rho \partial_j \rho \right\} + \frac{\Delta t}{2} v_k \partial_k [\partial_j (v_j U_i) + \partial_j P_{ij} - \rho g_i] \right\}^n .
\end{aligned}
\tag{A1}
$$

Here, U is the mass flux and superscripts denote the time step. The viscosity term is calculated implicitly for U^* to increase the stable time step also for viscosity-dominated flows.

Next, the correction is made for the mass flux. It involves calculating the density and energy fields at time step $n + 1$ using the predictor mass flux U^*. Since the pressure is determined by density and temperature fields, we could consider the pressure in Eq. (15) merely a shorthand and solve for density and temperature equations. This straightforward approach is not convenient, however, for two reasons. First, in our finite

element formulation all variables are approximated with a linear approximation function. Since higher-order derivatives appear in the derivative of stresses we need to introduce additional variables in order to evaluate the derivatives of stresses. Second, for our boundary conditions we need to impose a Dirichlet boundary condition for the pressure at the open boundary. This is greatly simplified by having the pressure as an additional variable in our system of equations. Thus, we split the equations such that the pressure tensor is an additional variable.

Inserting the correction of the mass flux to the density and temperature equations gives the correction step. The flux correction step is

$$U_i^{n+1} - U_i^* = \Delta t \big[\partial_j P_{ij}^{n+1} - \partial_j P_{ij}^n \big], \qquad (A2)$$

where P^{n+1} needs to be determined and depends on ρ^{n+1} and T^{n+1}. The correction step involving the pressure, density, and temperature equations is

$$
\begin{aligned}
P_{ij}^{n+1} = \Big[& p(\rho^m, T^m) - \kappa \rho^m \partial_k{}^2 \rho^m - \frac{1}{2} \kappa \partial_k \rho^m \partial_k \rho^m \\
& + \frac{\rho^m}{T^m} \partial_k \rho^m \partial_k T^m \Big] \delta_{ij} + \kappa \partial_i \rho^m \partial_j \rho^m,
\end{aligned}
\qquad (A3)
$$

$$\rho^{n+1} = \rho^n - \Delta t \, \partial_j \big[U_j^* - \Delta t \big(\partial_k P_{jk}^{n+1} - \partial_k P_{jk}^n \big) \big], \quad (A4)$$

$$
\begin{aligned}
e(\rho^{n+1}, T^{n+1}) = e(\rho^n, T^n) + \Delta t \Bigg\{ & -\partial_j \left[e(\rho^m, T^m) \frac{U_j^*}{\rho^m} \right] \\
& - \left[P_{jk}^{n+1} \partial_k \left(\frac{U_j^*}{\rho^m} \right) \right] + \alpha_0 \partial_j (\rho^m \partial_j T^m) \\
& + \eta_0 \left[\partial_j \left(\frac{U_k^*}{\rho^m} \right) + \partial_k \left(\frac{U_j^*}{\rho^m} \right) \right] \partial_j \left(\frac{U_k^*}{\rho^m} \right) \Bigg\}.
\end{aligned}
$$
$$(A5)$$

The above correction step can be taken in two different ways depending on the choice of the time step m used. If we use the previous time step in the correction step ($m = n$) then each of the above equations can be straightforwardly solved. If we instead use an implicit method ($m = n + 1$) then the above equations need to be solved together as a coupled set and each depends on the solution of the others. The implicit method leads to a significant increase in the maximal stable time step of the method, but the coupled solution is computationally expensive.

By numerical trial we find that the implicit method is advantageous when the liquid-gas interface is far from the walls of the computational domain. The larger time step gained by the implicit method is lost when a contact line is present in the system, however, and the explicit method is found to be computationally more efficient.

To summarize, the CBS solution method starts by taking a predictor step (A1) for the intermediate mass flux U^*. Then a corrector step (A3)–(A5) gives the density and temperature at the new time step. Finally, the mass flux, and thus velocity, at the new time step is obtained by the flux correction (A2).

By numerical trial we put the limit of the feasibility of the present implementation at temperatures $T \geqslant 0.7 T_c$. The lower below the critical point we quench the system the higher all the contrasts between the phases become, and the harder is the

numerical task. Consider the CFL condition with the highest speed in the system [i.e., the speed of sound in the liquid phase, which at the limit is $v_c(T = 0.7 T_c) \approx 3.15$], and the smallest element mesh size when adapted to the interface, which is $\Delta x \approx 0.1$. Our implicit solution method works with time step $\Delta t = 0.5$ under these conditions, whereas the explicit method needs $\Delta t = 0.01$. Referred to these the CFL number of the implicit method is CFL ≈ 16, and the explicit CFL ≈ 0.3. These CFL numbers offer a guideline to the numerical method, but recall that we are not attempting to correctly resolve the time evolution of the compressibility waves in this study. However, we do desire that the acoustic modes present in the compressible hydrodynamic equations do not make our numerical solver diverge.

APPENDIX B: ESTIMATE OF CRITICAL SHRINKING OR GROWING BUBBLE

The change in Gibbs free energy of the system upon a local increase of bubble radius can be used to predict whether a bubble of given size immersed in superheated liquid will shrink or grow, assuming the system will evolve in the direction of locally decreasing Gibbs free energy. The Gibbs free energy density is the Helmholtz free energy plus the pressure, where we can shift zero of Gibbs to remove ambient pressure, leaving only the Laplace pressure:

$$g = f + \Delta p. \qquad (B1)$$

Considering an isothermal system at temperature T we have the coexistence gas and liquid densities ρ_g and ρ_l. Assuming an initial condition of a bubble of radius r immersed in metastable liquid at density $\rho_{\text{ext}} < \rho_l$, the system can decrease its Helmholtz free energy by increasing the bubble size, thereby phase separating some of the metastable liquid to the coexistence densities. However, this costs free energy in interface tension as the bubble circumference grows, which is
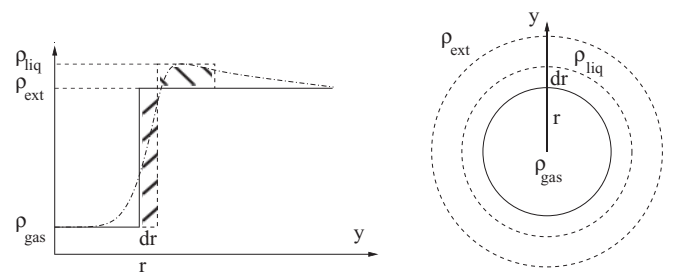

FIG. 13. Schematic to estimate whether a bubble immersed in metastable liquid will locally gain or lose Gibbs free energy by growing. On the left-hand side initially the bubble density profile is thought to be the solid line, with proper interface tension associated with the sharp interface. Growing the bubble by dr causes the metastable liquid to phase separate to liquid and gas (as per coexistence at this temperature), thereby gaining free energy. The result of the bubble growing is the dashed line with a square hump at the interface. Shaded boxes are of equal area for mass conservation. Curved dash-dotted line schematically shows how the density profile actually looks numerically with a bubble and an open bound, showing the approximate nature of the estimate. The right-hand side is the potentially growing bubble shown from above, with the one-dimensional profile cut shown.

taken into account by integrating $\Delta p \propto r^{-1}$ over the bubble area $\propto r^2$. Local mass conservation determines how much liquid is created for every unit of gas. Increasing the size of the gas bubble from r to $r + \Delta r$, the Gibbs free energy changes by

$$
\Delta G = \pi \sigma \Delta r + 2\pi r \Delta r \left\{ [f(\rho_g, T) - f(\rho_{\text{ext}}, T)] \right.
$$
$$
\left. + \frac{\rho_{\text{ext}} - \rho_g}{\rho_l - \rho_{\text{ext}}} [f(\rho_l, T) - f(\rho_{\text{ext}}, T)] \right\}, \qquad \text{(B2)}
$$

where $(\rho_{\text{ext}} - \rho_g)/(\rho_l - \rho_{\text{ext}})$ is the amount of metastable liquid turned to coexistence liquid for every unit of metastable liquid turned to coexistence gas according to

mass conservation, which is obeyed locally at the bubble circumference even though the system can exchange mass at an open boundary. Considering where ΔG changes sign upon positive Δr, we predict the critical radius of the bubble that will neither grow nor shrink to be

$$
r_{\text{crit}}^{\text{pred}} = -\frac{\sigma}{2} \left\{ [f(\rho_g, T) - f(\rho_{\text{ext}}, T)] \right.
$$
$$
\left. + \frac{\rho_{\text{ext}} - \rho_g}{\rho_l - \rho_{\text{ext}}} [f(\rho_l, T) - f(\rho_{\text{ext}}, T)] \right\}. \qquad \text{(B3)}
$$

This estimate and how it approximates the numerical density profiles is illustrated in the schematic in Fig. 13.

[1] V. K. Dhir, Annu. Rev. Fluid Mech. **30**, 365 (1998).
[2] T. G. Theofanous, T. N. Dinh, J. P. Tu, and A. T. Dinh, Exp. Therm. Fluid Sci. **26**, 775 (2002).
[3] T. G. Theofanous, J. P. Tu, A. T. Dinh, and T. N. Dinh, Exp. Therm. Fluid Sci. **26**, 775 (2002).
[4] H. T. Phan, N. Caney, P. Marty, S. Colasson, and J. Gavillet, C. R. Mecanique **337**, 251 (2009).
[5] V. S. Nikolayev, D. Beysens, Y. Garrabos, C. Lecoutre, and D. Chatain, Microgravity Sci. Technol. **18**, 34 (2006).
[6] V. S. Nikolayev, D. Chatain, Y. Garrabos, and D. Beysens, Phys. Rev. Lett. **97**, 184503 (2006).
[7] D. M. Anderson, G. B. McFadden, and A. A. Wheeler, Annu. Rev. Fluid Mech. **30**, 139 (1998).
[8] A. Onuki, Phys. Rev. E **75**, 036304 (2007).
[9] G. Tryggvason, B. Bunner, A. Esmaeeli, and N. Al-Rawahi, Adv. Appl. Mech. **39**, 81 (2003).
[10] V. S. Nikolayev and D. A. Beysens, Europhys. Lett. **47**, 345 (1999).
[11] J. D. Van der Waals, Verh.-K. Ned. Akad. Wet., Afd. Natuurkd., Eerste Reeks **1**, 56 (1893); J. S. Rowlinson, J. Stat. Phys. **20**, 197 (1979).
[12] D. Korteweg, Arch. Neerl. Sci. Exactes Nat. Ser II **6**, 1 (1901).
[13] V. L. Ginzburg and L. D. Landau, Zh. Eksp. Teor. Fiz. **20**, 1064 (1950).
[14] J. W. Cahn and J. E. Hilliard, J. Chem. Phys. **28**, 258 (1958).
[15] J. E. Dunn and J. Serrin, Arch. Ration. Mech. Anal. **88**, 95 (1985).
[16] D. Jacqmin, J. Comput. Phys. **155**, 96 (1999).

[17] R. Teshigawara and A. Onuki, Phys. Rev. E **82**, 021603 (2010).
[18] A. Pecenko, J. G. M. Kuerten, and C. W. M. van der Geld, Int. J. Multiphase Flow **36**, 558 (2010).
[19] A. Pecenko, L. G. M. van Deurzen, J. G. M. Kuerten, and C. W. M. van der Geld, Int. J. Multiphase Flow **37**, 149 (2010).
[20] S. Merabia and I. Pagonabarraga, Eur. Phys. E **20**, 209 (2006).
[21] R. Teshigawara and A. Onuki, e-print arXiv:1108.0213v1 (2011).
[22] T. Colonius, Annu. Rev. Fluid Mech. **36**, 315 (2004).
[23] P. Nithiarasu, R. Codina, and O. C. Zienkiewicz, Int. J. Numer. Meth. Engng. **66**, 1514 (2006).
[24] O. C. Zienkiewicz *et al.*, *The Finite Element Method for Fluid Dynamics*, 6th ed. (Elsevier, 2005).
[25] G. Amberg, R. Tonhardt, and C. Winkler, Math. Comput. Simul. **49**, 149 (1999).
[26] M. Do-Quang, W. Villanueva, I. Singer-Loginova, and G. Amberg, Bull. Pol. Acad. Sci-Te **55**, 229 (2007).
[27] P. Yuan and L. Schaefer, Phys. Fluids **18**, 042101 (2006).
[28] W. Villanuava and G. Amberg, Int. J. Multiphase Flow **32**, 1072 (2006).
[29] P. Papatzacos, Phys. Scr. **61**, 349 (2000).
[30] H. J. Palmer, J. Fluid Mech. **75**, 487 (1976).
[31] L.-T. Kong, D. Vriesinga, and C. Denniston, Europhys. Lett. **93**, 50004 (2011).
[32] A. Carlson, D.-Q. Minh, and G. Amberg, Phys. Fluids **21**, 121701 (2009).